Speed of free convective fingering in porous media

Yueqing Xie,[1,2] Craig T. Simmons,[1,2] and Adrian D. Werner[1,2]

[1]   Previous studies have examined free convection and the development of fingers in variable-density groundwater environments, but the penetration rates of fingering processes (i.e., fingering speeds) have not been systematically investigated. Unlike common groundwater processes driven by advection and whose flow rates may be computed using Darcy's law, fingering speeds are far less intuitive. In this study, fingering speeds are analyzed in a natural convection system using two measurable diagnostics: deepest plume front (DPF, providing upper bounds on plume speeds) and vertical center of solute mass (COM, providing global speeds). The permeability, porosity, and dispersion (longitudinal and transverse dispersivities) were varied using a perturbation-based stochastic approach to investigate their effects on fingering speeds. Modeling results show that the characteristic convective velocity, commonly used to represent theoretical fingering speeds, needs to incorporate effective porosity in a similar fashion to hydraulically driven average linear velocity and needs to be further adjusted by multiplying by a corrective factor f for predicting various fingering behaviors (approximately $f = 0.115$ for DPF and $f = 0.034$ for COM) in this study. A stochastic analysis demonstrates small variability in the time-varying speed of both DPF and COM between model realizations. This indicates that reproducing fingering speeds is likely to be achieved and that one single realization can adequately produce f for the characteristic convective velocity. This study also identifies that f for speeds of DPF is most likely to be constrained by (0.115, 1.000), which is extremely useful in the design of laboratory and field experimentation.

1.   Introduction

[2]   Many hydrogeologic situations may involve potentially unstable stratification where dense fluid sits above less dense fluid because of variations in solute concentration, temperature, and/or pressure of groundwater. Under certain conditions involving solutes, this stratification may lead to the development of gravitational instabilities (i.e., fingers or plumes) associated with free convection and subsequently cause solute transport over larger areas within shorter time scales than diffusion alone [e.g., *Wooding et al.*, 1997; *Zimmermann et al.*, 2006; *Zhang and Schwartz*, 1995; *Simmons*, 2005]. When fingers develop at the bottom edge of the interface between intruding dense water and ambient groundwater, they migrate downward and become entrained within the ambient groundwater flow [e.g., *Schincariol and Schwartz*, 1990; *Oostrom et al.*, 1992; *Wooding et al.*, 1997]. The rate and extent of groundwater contamination due to free convection are inherently linked to the descent speed of the solute fingers associated with the free convection process.

[3] Theoretical free convective fingering speeds have been associated previously with a generalized characteristic convective (Darcy) velocity $\mathbf{U_c}$, expressed as [*Gebhart et al.*, 1988; *Wooding et al.*, 1997; *Riaz et al.*, 2006]

$$\mathbf{U_c} = \frac{k\Delta\rho g}{\mu} = K\frac{\Delta\rho}{\rho_0}, \qquad (1)$$

where k is the permeability of a porous medium, $\Delta\rho$ is the density difference between maximum density and base reference density, g is the gravitational acceleration, μ is the dynamic viscosity, often assumed to be independent of solute concentration, K is the hydraulic conductivity of a porous medium, and ρ_0 is the base reference density. $\mathbf{U_c}$ has also been used in defining scaling relationships that assist in simplifying the complicated and nonlinear behavior associated with free convection.

[4] However, there has been ambiguity with regard to the use of effective porosity ε for computing free convective fingering speeds in hydrogeologic practice. For example, *Juster et al.* [1997] and *Post and Kooi* [2003] include ε in characterizing rates of plume migration, while *Wooding et al.* [1997], *Riaz et al.* [2006], and *Stevens et al.* [2009] neglect ε in their analyses of plume migration rates. A characteristic convective velocity $\mathbf{V_c}$, which is analogous to average linear velocity associated with advection processes, would be derived if ε is important (see Appendix A). There is a need to investigate further the effect of ε on plume

---

[1]National Centre for Groundwater Research and Training, Flinders University, Adelaide, South Australia, Australia.
[2]School of the Environment, Flinders University, Adelaide, South Australia, Australia.

migration rates, particularly given that ε is a component of the dimensionless Rayleigh number Ra, which characterizes the onset of free convection and indicates the extent of instability. Ra is given by

$$Ra = \frac{gk\Delta\rho H}{\mu\varepsilon D_0} = \frac{\mathbf{U_c}H}{\varepsilon D_0},$$ (2)

where H is the height of a porous layer and D_0 is the molecular diffusion coefficient. Therefore, whether $\mathbf{U_c}$ or $\mathbf{V_c}$ is more representative of theoretical free convective fingering speeds still remains unclear in the literature.

[5] Furthermore, how $\mathbf{U_c}$ or $\mathbf{V_c}$ relates to the real fingering speeds (what one observes in practice) also remains unclear. Importantly, unlike advection processes in groundwater whose speeds can be routinely computed using the classic Darcy's law (no density effect) and that are therefore relatively intuitive once the hydraulic conductivity and hydraulic head data in the system are known, the same is not true of the speeds of free convection. There is no universally accepted way of computing the speed of free convection phenomena, and in comparison to advection, our intuition regarding how fast free convection processes are in real groundwater systems is clearly lacking. Critically, whether the speeds of free convective fingering are reproducible and amenable to prediction remains unresolved. These are extremely important matters both for interpreting laboratory, model, and field experiments and in enhancing our ability to make robust predictions about free convection processes in those settings. An understanding of the speed of free convection processes will also be critical in monitoring systems designed to measure and monitor time-dependent behavior of free convection processes, associated with a large range of environmental phenomena, in the field. These matters require resolution and a systematic and quantitative evaluation.

[6] *Post and Kooi* [2003] conducted numerical experiments to examine the real fingering speeds associated with salinization of coastal aquifers due to free convection. They employed a representative homogeneous free convective system ($Ra = 6000$) with seawater continuously intruding into groundwater from the top as their base model. The permeability was then varied to investigate the corresponding variation in fingering speeds. By analyzing three horizontally averaged salinity fractions (0.1, 0.3, and 0.5, where a value of 1 represents seawater) in the series of numerical runs, they discovered that the permeability of an aquifer matrix directly influenced the rate of plume descent. They also generalized an empirical equation of plume descent rates that are given by an upper bound defined by 0.22 $\mathbf{V_c}$. They noted that their empirical equation is only approximate because of the limitations arising from various assumptions (e.g., neglecting mechanical dispersion).

[7] Other studies have also demonstrated fingering speeds using different approaches, e.g., mean amplitude of fingers [*Wooding*, 1969], the advance of fastest finger tip [*Riaz et al.*, 2006], and the average depth of deepest fingers [*Simmons et al.*, 2002]. *Wooding*'s [1969] Hele-Shaw cell results show the growth of mean amplitude of unstable waves is a function of 0.446 $\mathbf{U_c}$ at an unstable diffusive interface. *Riaz et al.* [2006] examined the stability of an unstable diffusive boundary layer relating to carbon dioxide

sequestration in numerical models, and *Simmons et al.* [2002] attempted to investigate the phenomena of free convective solute transport in sand tank experiments. Both *Riaz et al.*'s [2006] theoretical study and *Simmons et al.*'s [2002] laboratory study qualitatively demonstrate that fingers tend to penetrate linearly with time after they develop from boundary layers, but no generic fingering speeds were identified. Although nonlinear penetration behaviors were observed by *Wooding et al.* [1969], *Post and Kooi* [2003], and *Riaz et al.* [2006] at the very early times, it is of greater importance to carefully reconcile these existing fingering speeds with both similarities and differences [*Wooding*, 1969; *Post and Kooi*, 2003] produced across various measurements, scale geometries, and hydrogeologic settings. We also need to systematically investigate the variability of fingering speeds with time, which has not been addressed previously, and can significantly assess the predictability of free convective fingering in inherently unstable free convection systems.

[8] The aim of this study is to reconcile the approaches for computing the speed of free convection that have been presented in the literature to date and to develop further intuition about the speed of free convection. We conducted a series of numerical simulations using the finite element subsurface code FEFLOW [*Diersch*, 2005] to examine the effects of different parameters on fingering speeds using the modified solute analogous Elder problem [*Xie et al.*, 2010] and two measurable diagnostics: deepest plume front (DPF, providing upper bounds on plume speeds) and vertical center of solute mass (COM, providing global speeds). The permeability, porosity, and dispersion (longitudinal and transverse dispersivities) were varied using a perturbation-based stochastic approach to investigate their effects on fingering speeds.

2. Mathematical Modeling

2.1. Natural Convection in a Closed Porous Medium

[9] The classic Elder problem was initially set up by *Elder* [1967] to investigate transient thermal convection in both laboratory experiments and numerical models. It was then modified into a solute analogous natural convection problem by *Voss and Souza* [1987] to benchmark variable density flow code SUTRA. Since then, it has become a well-studied typical example of natural convection phenomena both for benchmarking numerical simulators [e.g., *Oldenburg and Pruess*, 1995; *Kolditz et al.*, 1998; *Ackerer et al.*, 1999] and for serving as a base case to investigate more complicated free convection problems [e.g., *Prasad and Simmons*, 2003; *Post and Prommer*, 2007]. It was adopted by *Xie et al.* [2010] to investigate the effect of time-variant solute loading upon natural convection in porous media. *Xie et al.* [2010] pointed out that the classic Elder problem is more relevant to natural salt lake settings [e.g., *Van Dam et al.*, 2009] because of the high density of the imposed solute (1,200 kg m^{-3}), equivalent to a salinity of 360,000 mg L^{-1} [*Adams and Bachu*, 2002]. In order to adjust the classic Elder problem to be more representative of natural settings, two significant modifications were made, which included replacing the thermal diffusion coefficient with solute hydrodynamic dispersion and changing the bottom concentration boundary condition to a no-solute

flux boundary condition. Consequently, the modified dispersive Elder problem demonstrated a large number of unstable fingers beneath the top boundary layer and is a more realistic example for solute-driven natural convection. The reader is referred to the work by *Xie et al.* [2010] for a detailed description of the modified dispersive Elder problem. In the current study, we adapted this dispersive Elder problem as our natural free convection base case by two slight modifications in order to weaken aquifer-scale circulation and shorten simulation times, as discussed in the rest of this section.

[10] In the dispersive Elder problem, *Xie et al.* [2010] still retained the middle half concentration boundary condition on the top from the solute analogous Elder problem [*Voss and Souza*, 1987] to supply solute to the groundwater system. This boundary condition may, for example, represent a salt lake above an extensive groundwater system. However, they found that this limited length of solute supply forms aquifer-scale circulation on the outer edges of the finite solute source. Fingers, generated from the top boundary layer, then not only migrate downward but move toward the vertical center. This centralizing phenomenon is likely to occur in salt lake settings [*Wooding et al.*, 1997; *Simmons et al.*, 1999] and to cause large aquifer-scale circulation associated with free convection. These large-scale circulations will also interfere with the speeds of the local-scale fingering phenomena. However, the objective of the current study is to conduct a systematic analysis of free convective fingering speeds, without the complicating effects of aquifer-scale circulation that occurs in the classic Elder problem. Therefore, a concentration boundary condition across the entire top boundary, similar to previous studies [e.g., *Post and Kooi*, 2003; *Riaz et al.*, 2006], was utilized in the current study to eliminate the effects of aquifer-scale circulation on free convective speeds and to therefore produce uncontaminated results.

[11] *Xie et al.* [2010] extended the vertical dimension of the classic Elder problem from 150 to 600 m to maximize opportunities to observe finger behavior. This large-scale model required long runtimes because of the increase in Ra induced by the extension of model depth. In the current study, numerical models were implemented stochastically (30 realizations for each case) in order to assess behavior in a statistical sense (discussed in section 2.6). In order to reduce runtimes, a smaller length scale of 100 m was adopted for both the horizontal and vertical dimensions of the model. The conceptual model for this modified Elder problem is shown in Figure 1, and the corresponding parameters that are required to simulate this case using FEFLOW are presented in case BASE in Table 1. The governing equations employed by FEFLOW are given in Appendix B. The current modified Elder problem employs a homogeneous and isotropic porous medium.

[12] The current natural convection system is characterized by $Ra = 3.4 \times 10^5$, which is much greater than the critical Ra of 0, the onset criterion of free convection in the classic Elder problem. This critical Ra of 0 was recently demonstrated by *van Reeuwijk et al.* [2009], who analyzed the solute flux behavior through the source zone in response to the variation in Ra. Their analysis indicates that a small presence of salt might trigger free convection. Vigorous physical instabilities are therefore expected because of this large Ra.
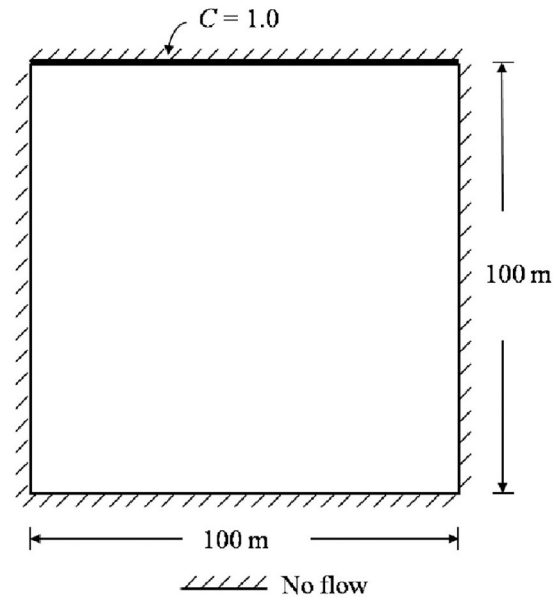

Figure 1. The geometry and boundary conditions of the natural convection in a closed system, adapted from *Xie et al.* [2010].

2.2. Numerical Experiments

[13] Ten experimental cases, each comprising 30 individual simulations, were designed to investigate the variation in fingering speeds in response to the change in three factors that may impact finger penetration, which are matrix permeability k, effective porosity ε, and mechanical dispersion D_β.

[14] Natural settings are typically characterized by wide ranges in k, thereby producing a wide spectrum of Ra values, indicating different degrees of physical instability. In order to examine the effect of k on fingering speeds at various extents of physical instability, k (MP1 and MP2 in Table 1) was chosen to be varied in a similar fashion to that done by *Post and Kooi* [2003].

[15] In solute transport ε plays an inverse role through void spaces in porous media, whereby small ε will cause faster groundwater movement and will subsequently allow a greater amount of solutes to flow. It may significantly influence fingering speeds if $\mathbf{V_c}$ is the appropriate quantity. Therefore, we wanted to carefully check the effect of ε, and ε was varied to two different values, 0.01 (EP1) and 0.4 (EP2) (Table 1), to clarify its role in fingering speeds. Note that even though $\varepsilon = 0.01$ is slightly unrealistic in accordance with the associated k value, it is still useful to test this value in a theoretical sense within the model.

[16] D_β is composed of two components, i.e., longitudinal dispersivity β_L and transverse dispersivity β_T [*Bear*, 1972]. In laboratory-scale Hele-Shaw cell or sand tank experiments of free convection, D_β is usually neglected [e.g., *Post and Simmons*, 2010] or assumed to be on the same order of magnitude as molecular diffusion [e.g., *Simmons et al.*, 1999] because of the small spatial scale and homogeneous settings. In a numerical experiment with a large length scale, D_β may have a strong impact on the evolution of descending fingers and should be taken into account. In order to identify

Table 1. Parameters Adopted in FEFLOW Simulations[a]

	Experimental Case									
	BASE	MP1	MP2	EP1	EP2	MD1	MD2	MD3	MD4	MD5
Model depth H (m)	100	...	...	...	...	...	...	...	...	...
Model length L (m)	100	...	...	...	...	...	...	...	...	...
Gravitational acceleration g (m s^{-2})	9.8	...	...	...	...	...	...	...	...	...
Dynamic viscosity μ (10^{-3} kg m^{-1} s^{-1})	1	...	...	...	...	...	...	...	...	...
Density difference $\Delta\rho$ (kg m^{-3})	200	...	...	...	...	...	...	...	...	...
Matrix permeability k (10^{-13} m^2)	4.85	0.485	48.5	...	...	...	...	...	...	...
Diffusion coefficient D_0 (10^{-9} m^2 s^{-1})	2.8	...	...	...	...	...	...	...	...	...
Longitudinal dispersivity β_L (m)	1	...	...	...	...	1	10	5	1	5
Transverse dispersivity β_T (m)	1	...	...	...	...	0.1	1	0.5	0.5	1
Effective porosity ε	0.1	...	...	0.01	0.4	...	...	...	...	...
Rayleigh number Ra (10^4)	34	3.4	340	340	8.5	...	...	...	...	...
Simulation time T (years)	10	50	1	1	10	10	10	10	10	10

[a]Experimental case names containing MP, EP, and MD refer to cases with changes in matrix permeability, effective porosity, and mechanical dispersion, respectively. A set of dots (...) indicates that the parameter is unchanged from that in case BASE.

the individual impact of both β_L and β_T, we reduced β_L by 1 order of magnitude (case MD1) and increased β_T by 1 order of magnitude (case MD2) on the basis of case BASE, according to the empirical relationship between longitudinal dispersivities and modeling length scales [*Schulze-Makuch*, 2005], as seen in Table 1.

[17] Note that the variation in parameters resulted in a wide spectrum of Ra, thereby causing different degrees of physical instability. It is expected that fingers in the different systems will therefore reach the bottom within various times. Because of the requirement of a stochastic implementation, time scales for various cases were allowed to vary accordingly in order to reduce total runtimes provided that the measurable diagnostic COM (section 2.5) can reach a relatively steady state. Therefore, we simulate case MP1 for 50 years, cases MP2 and EP1 for 1 year, and all other cases for 10 years, as noted in Table 1.

2.3. Random Perturbations

[18] In real-world groundwater systems, unstable fluid flow is usually triggered by geologic heterogeneity and/or fluid heterogeneity, e.g., pore-scale and regional-scale heterogeneities in permeability distribution, small variations in salinity due to irregular evaporation and surface temperature. Hence, it is expected that such perturbations may be spatiotemporally variable. They are also extremely difficult, if not impossible, to quantify in practice.

[19] However, in groundwater modeling, triggering physical instabilities is often reliant on numerical perturbations arising from local truncation and round-off errors. This dependency is often unreliable and uncontrollable because those numerical perturbations are unrealistic and not easily quantified. *Horne and Caltagirone* [1980] called for the consideration of small nondeterministic perturbations to overcome the seemingly perfect mathematical solutions to nonlinear problems in a numerical study of examining the effect of triggering physical instabilities in thermal convection plume patterns. Numerical simulations [e.g., *Simmons et al.*, 1999; *Post and Simmons* 2010] have shown that fingers are initiated from outer edges of a solute boundary and are different from laboratory observations without considering small perturbations across the boundary layer. Hence, random perturbations were incorporated to trigger early time free convective behavior along the

boundary layer. A small random perturbation function was added to the entire top concentration boundary in order to better represent random system behavior and trigger physical instabilities [e.g., *Simmons et al.*, 1999; *Riaz et al.*, 2006]. The perturbation function is adopted from *Simmons et al.* [1999] and is given by

$$C_{\text{node}}(t) = C_{\text{dense}} + \frac{1}{100}(C_{\text{dense}} - C_0)[\text{rand}\,(t,0) - 0.5]\,(0 < t < T),$$
(3)

where $C_{\text{node}}(t)$ is the normalized concentration of a node at the top boundary at time t, C_{dense} and C_0 are the normalized concentrations of dense water and base reference water, respectively, rand $(t,0)$ is a random function used for generating fractions uniformly distributed between 0 and 1, and T is the total simulation time depending on modeling cases. A systematic comparison of the results associated with different amplitudes of perturbations (0%, 0.5%, 1%, and 2%) indicates that this perturbation amplitude (0.5%) is sufficiently small and reasonable to trigger fingers at early stages without leading to strong influence at later stages. This random perturbation was implemented in all simulations.

[20] Because of the density effect, each free convective system is characterized by multiple solutions such that fingering speeds have slight variability. In order to rigorously analyze the general trends of fingering speeds and the corresponding variability, statistical results (i.e., mean and standard deviation) are computed. The incorporation of the random perturbation method is a critical precursor to using the necessary stochastic approach, which is described further in section 2.6.

2.4. Spatial and Temporal Discretization

[21] It is commonly recognized that adequate grid sizes and time steps are necessarily required to minimize numerical perturbations and dispersion that arise from truncation and round-off errors. The common criterion to determine grid discretization is the mesh Péclet number $Pe \approx \Delta L/\beta_L$ < 2 [*Diersch and Kolditz*, 2002], where ΔL is the transport distance between two sides of an element measured in the direction of groundwater flow and β_L is the longitudinal dispersivity. In the current study, rectangular cells are used, and the discretization comprises $\Delta x = 0.5$ m horizontally

and $\Delta y = 0.25$ m ($0 < y < 10$ m) and $\Delta y = 0.5$ m ($y > 10$ m) vertically. This discretization scheme produces 44,421 nodes, 44,000 elements, and a maximum Pe of about 0.5. This level of discretization achieved grid convergence based on several macroscopic diagnostics, including total solute mass, vertical center of solute mass, and solute flux across the top solute mass boundary, and is used in all simulations. A fully implicit, varying time-stepping scheme, allowing manually specified time steps, was applied to numerical models [*Diersch*, 2005]. An initial time step of 0.01 day and a maximum time step of 1 day were utilized to restrict the time-stepping scheme. The selection of specific time steps in each case is relatively arbitrary but was modified accordingly to ensure mathematical convergence was achieved.

2.5. Measurable Diagnostics

[22] A highly unstable system is characterized by an oscillatory regime where occurrence and disappearance of physical instabilities may occur continuously [*Diersch and Kolditz*, 2002]. It is therefore difficult to trace the movement of one single finger, which might coalesce with other fingers or disappear due to a reduction in solute reinforcement. More reliable characteristics are required to represent a continuous descending behavior of fingers. Previous studies have demonstrated that different diagnostics may result in differing fingering speeds. In the current study, in order to present a thorough analysis, we adopted two diagnostics, DPF [e.g., *Riaz et al.*, 2006] and COM [e.g., *Prasad and Simmons*, 2003], to analyze behavior.

[23] DPF is the deepest position of the interface between the intruding solute plume and ambient groundwater and is defined using the concentration of $C = 0.01$. COM is the vertical center of mass of the salt plume and is integrated across the entire model domain (Appendix C). Both diagnostics are measured from the top of the domain. It is expected that COM provides a slower but more reliable fingering speed than DPF because of its integrating effect. Note that *Post and Kooi*'s [2003] empirical results indicate that fingering speeds (defined in a similar fashion to DPF) decrease with an increase in the concentration of measured isochlors. However, we intend to analyze the upper bound on the spectrum of fingering speeds and have therefore chosen a very small, but discernible, concentration value for analysis. After systematically comparing fingering speeds for a number of isochlors in a few test runs, we found $C = 0.01$ represents a reliable indicator of the upper bound of the spectrum of fingering speeds.

[24] Fingering speeds can be analyzed through linear approximation by finding the best fitted straight lines in DPF-time and COM-time graphs. We use U_{DPF} and U_{COM} to represent the linearly approximated fingering speeds from DPF and COM, respectively. It should be noted that U_{DPF} and U_{COM} can only give constant fingering speeds in each realization because of the limitation of the approach and cannot explicitly demonstrate the variation in speeds. Hence, we consider the instant speeds of DPF and COM (i.e., SDPF and SCOM, Appendix C) at different times by calculating the finite difference derivative of these variables over time. The terms instantaneous speed of DPF (SDPF) and instantaneous speed of COM (SCOM) are used to distinguish the derivative approach from the linear

approximation approach. In the stochastic study (discussed in section 2.6), SDPF and SCOM are capable of evaluating the time-varying general trends of fingering speeds and their corresponding variability.

2.6. Stochastic Implementation

[25] The complicated nature of fingering processes leads to differences between fingering realizations, and hence, multiple realizations are needed to develop a sense of the variability that might be encountered because of this randomness. A stochastic approach was utilized in this study to evaluate fingering speeds in a statistical sense. Since the random perturbation function was imposed to the entire top boundary, running one specific case at different times can obviously produce different solutions and fingering speeds. Therefore, one model can be implemented 30 times in order to obtain a distribution of results as per *Prasad and Simmons* [2003]. According to probability theory [*Kreyszig*, 1988], 30 samples can yield a confidence interval of plus or minus two standard deviations ($\pm 2\sigma$) at a confidence level of 95%. A relatively small standard deviation across stochastic simulation sets indicates small variability and high reproducibility of fingering speeds. It was expected that variability in COM would be smaller than the variability in DPF because of the integrating effect of the former diagnostic. Note that the stochastic results do not present the exact behavior of fingering speeds, but rather demonstrate the overall trends represented by the mean values (μ_{SDPF} and μ_{SCOM}) and the corresponding variability as represented by standard deviations (σ_{SDPF} and σ_{SCOM}).

3. Results and Discussion

3.1. A Preliminary Analysis

[26] Figure 2 demonstrates the comparison of DPF development of $C = 0.01$ to $C = 0.1$, 0.2, and 0.6 in one realization of case BASE. Although $C = 0.01$ is an order of magnitude smaller than $C = 0.1$ and 0.2, the corresponding behavior of DPF is quite similar to others and is characterized by approximately linear descent. DPF of $C = 0.6$, however, demonstrates strong oscillation due to fluid entrainment before starting to descend linearly at around 5 years. It becomes clear that DPF of $C = 0.01$ is more reliable and adequate to capture the advance of fingers and provide stable results.

[27] Figure 3 compares the behavior of DPF in cases with different perturbations, grid discretization, and length scales. Results show very close trends to case BASE (Figure 5a) and therefore indicate that our current setting is appropriate to carry out simulations with reasonable accuracy.

[28] Plume patterns from five realizations in case BASE and at various simulation times are illustrated in Figure 4. Plume patterns are clearly different between simulations because of the inherent randomness, as expected. However, DPF seems to reach a relatively consistent depth across the five simulations at any specific time. After the salt plume reached the bottom no-flow boundary, the system started to fill with solute, and COM tended toward a steady state value. This characteristic of free convective behavior that we observed in our study is in agreement with simulations of CO_2 sequestration in a deep aquifer performed by *Moortgat et al.* [2011], who developed a higher-order numerical method for multiphase flow.
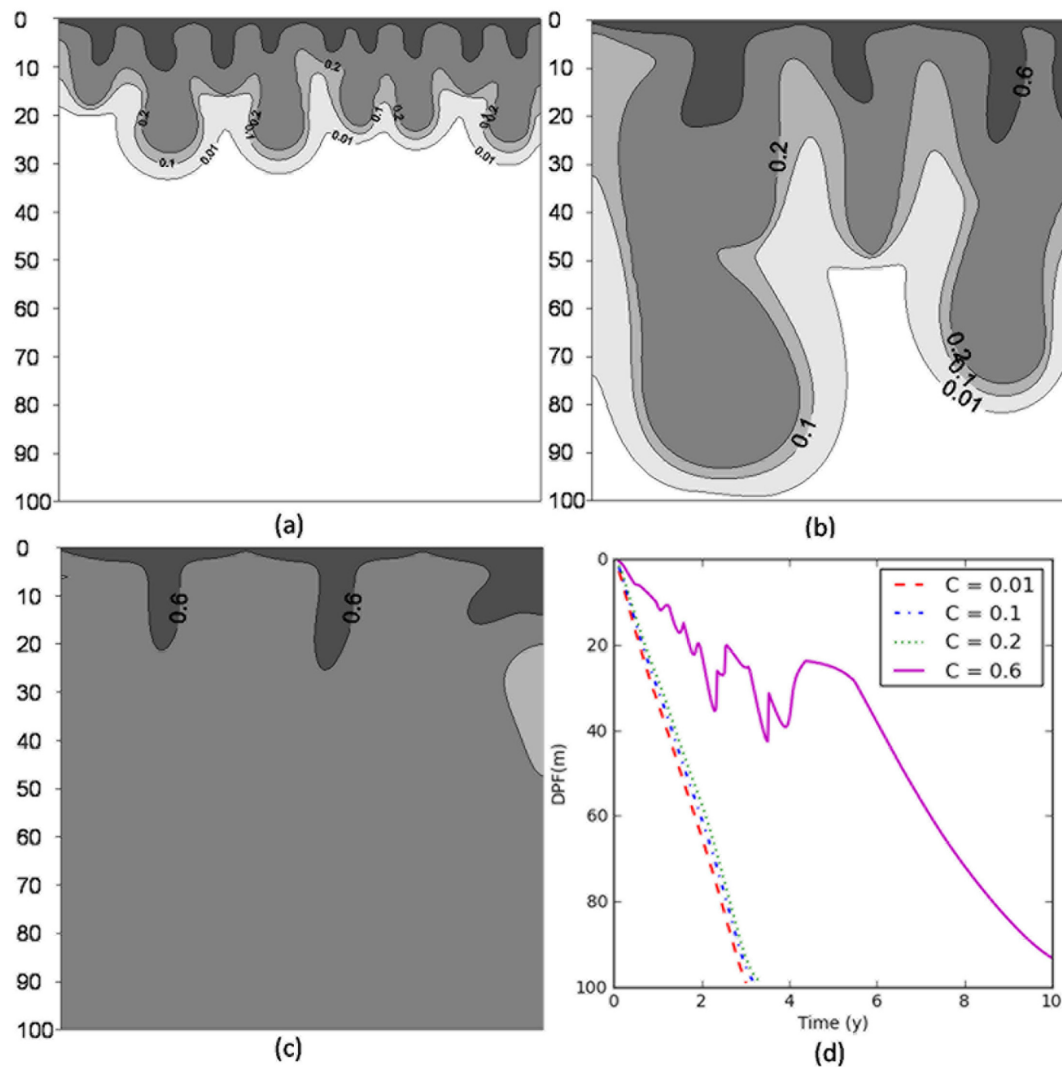
Figure 2. The development of fingering speeds based on four different *C* values (i.e., 0.01, 0.1, 0.2, and 0.6). Isochlors at (a) 0.98, (b) 3.01, and (c) 5.01 years. Gray color scales are used to assist in distinguishing different isochlors. (d) The evolution of DPF with time for all *C* values.

[29] Variation in fingering speeds, however, can be observed both within and between models. DPF in Figure 4c, for instance, was slightly deeper than in Figure 4b at both 0.85 and 1.75 years, but the relation was reversed at 2.85 years. This is because large structures were formed later in Figure 4b to strengthen the finger penetration, whereas fingers in Figure 4c were comparatively discrete and independent such that they appeared to move at a stable speed. Fingering speeds of individual fingers within a model appeared to be more complicated because of strong circulation associated with free convection. Fingers may diminish because of coalescence with a neighboring finger, forming a bigger one (e.g., finger number decreased dramatically from 19 at 0.27 years to 9 at 0.85 years in Figure 4a), or may become retarded because of upwelling effects from nearby fingers (e.g., the finger in the vertical center in Figure 4e did not penetrate much from 1.75 to 2.85 years). This clearly demonstrates that it is difficult (and virtually impossible) to quantify fingering speeds by measuring the

descent of every individual finger because of a strong free convective process, and therefore, some commonly used and easily accessed plume characteristics, such as DPF and COM adopted in this study, are, indeed, required to represent the speed of free convective fingering.

[30] Figure 5 illustrates the evolution of DPF and COM and the corresponding SDPF and SCOM of the case illustrated in Figure 4a. On the whole, DPF and COM present approximately linear trends, except that later COM behavior asymptotically approaches the vertical center of the groundwater system because of the accumulation of salt in the system as the model domain begins to fill up with salt (Figure 5a). By fitting straight lines to both DPF-time and COM-time curves, we determined constant representative fingering speeds as follows: 36 m yr^{-1} for DPF and 12 m yr^{-1} for COM.

[31] In contrast, SDPF and SCOM in Figure 5b reveal that fingering speeds of physical instabilities are not simply near linear but are rather oscillatory throughout the
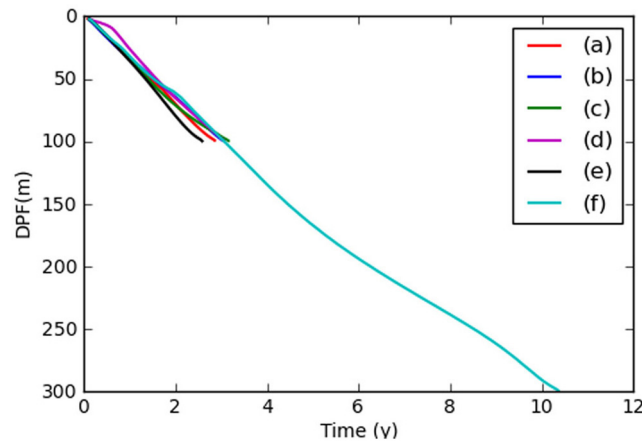
Figure 3. Comparison of deepest plume front (DPF) versus time: curve a, a realization of case BASE with 0.5% random perturbation to the top boundary condition; curve b, same as curve a except no random perturbation; curve c, same as curve a except 1% random perturbation; curve d, same as curve a except globally refined grid elements; curve e, same as curve a except double lateral length scale; curve f, same as curve a except double vertical length scale.

simulation, as also seen in the work by *Post and Kooi* [2003]. Four important stages can be observed from the behavior of SDPF in Figure 5b. At early times, SDPF increased briefly in the process of finger formation to 40 m yr^{-1} at around 0.27 years, followed by progressive reduction mainly due to the reduction of the density contrast between the finger and ambient groundwater induced by dispersion and diffusion effects, as explained by *Post and Kooi* [2003]. Surprisingly, after about 1.75 years, SDPF suddenly increased back to a high fingering speed (43 m yr^{-1}) before gradually dropping again because of both the dispersion-diffusion effect and the bottom boundary effect. The cause of the sudden increase was that another finger overtook the leading position of the current one because of stronger penetration capability (comparing plume patterns at 1.75 and 2.85 years in Figure 4a). Finger coalescence is also likely to result in the same increase in SDPF, both in other realizations (not shown here) and as seen by *Post and Kooi* [2003]. After DPF reached the bottom, causing the termination of SDPF, solutes started to accumulate in the system and subsequently led to the decrease in SCOM to zero (i.e., the system stabilized), as expected. Overall, the variation in SCOM is less oscillatory than SDPF because of its integrating effect.

[32] From the comparison, it is clear that the linear approximation can be used to make an approximate assessment of the fingering speeds in a free convective groundwater environment and to further evaluate the speed of aquifer contamination. But such an approximation obviously leaves out the details of time-varying fingering speeds. For the purpose of exploring the variability of fingering speeds, the detailed SDPF and SCOM diagnostics were considered.

3.2.　The Effect of Permeability *k*

[33] Figure 6 shows the development of means and standard deviations of both SDPF and SCOM in cases BASE

($k = 4.85 \times 10^{-13}$ m^2), MP1 ($k = 4.85 \times 10^{-14}$ m^2), and MP2 ($k = 4.85 \times 10^{-12}$ m^2). As a whole, Figure 6 clearly shows that the increase in k causes both SDPF and SCOM to increase by the same magnitude when comparing the magnitude of vertical axes of three graphs; μ_{SCOM} appears to be more stable and reliable than μ_{SDPF} because of its smoother trend and smaller variation in the corresponding standard deviation.

[34] Two evident features can be observed at early and later times from the behavior of μ_{SDPF}. At early times (i.e., the processes of finger formation), μ_{SDPF} gradually increases because of the penetration of the boundary layer followed by the formation of unstable fingers, as expected. Furthermore, μ_{SDPF} seems to be somewhat sensitive to the small random perturbations at the commencement of each case in comparison to later time behavior and therefore produces minor oscillations in Figures 6a and 6b. Initial oscillation is not observed for μ_{SDPF} in Figure 6c because fingers formed rapidly in case MP2 because of the stronger nonlinear dynamics associated with the higher *Ra* of 3.4×10^6. At later times, μ_{SDPF} in Figure 6 demonstrates globally decreasing trends because of the reduction of the density difference between fingers and ambient groundwater induced by diffusive-dispersive losses and the growing influence of the bottom boundary, which retards free convection. It should be noted that an apparently short-lived increase in μ_{SDPF} can be observed at around 11 years in Figure 6a, caused by the formation of large structures. In comparison, μ_{SDPF} in Figure 6c shows a rapid rise to 450 m yr^{-1} at around 0.06 year as a result of finger coalescence and a subsequent quick recovery, most likely due to the influence of other competitive fingers.

[35] In contrast, μ_{SCOM} in Figure 6 shows similar behavior (i.e., an increase) to μ_{SDPF} at early times but different (i.e., short-lived decrease followed by longer-lived increase) at later times before fingers reached the bottom. The short-lived decrease is mainly caused by lateral finger interaction, which slows down the overall vertical penetration, whereas the following longer-lived increase is attributed to the continuous solute injection, which either forms new fingers or reinforces existing fingers. Apparently, the bottom boundary effects do not have as strong an influence on COM as they do on DPF. Because of the restriction of fluid to flow outside of the system, solute starts to accumulate within the system after fingers reach the bottom. This process causes the decrease in SCOM asymptotically to 0 m yr^{-1} and the gradual reduction of solute flux entering the system through the top boundary.

[36] Note that Figure 6 demonstrates the same general trends of each diagnostic in all three cases irrespective of k values. This feature confirms that speed of free convective fingering is a linear function of k as shown in $\mathbf{U_c}$ (or $\mathbf{V_c}$). This feature is also consistent with the simple comparison of DPF based on one realization of each case (Figure 7). DPF in cases MP1, BASE, and MP2 reaches the system bottom at 27.5, 2.84, and 0.290 years, respectively, and therefore produces corresponding fingering speeds at 3.78, 36.0, and 335 m yr^{-1} through linear approximation, with about an order of magnitude difference.

[37] Both σ_{SDPF} and σ_{SCOM} in Figure 6 illustrate the variability of SDPF and SCOM at every time step. Neither σ_{SDPF} nor σ_{SCOM} presents obvious trends of variability
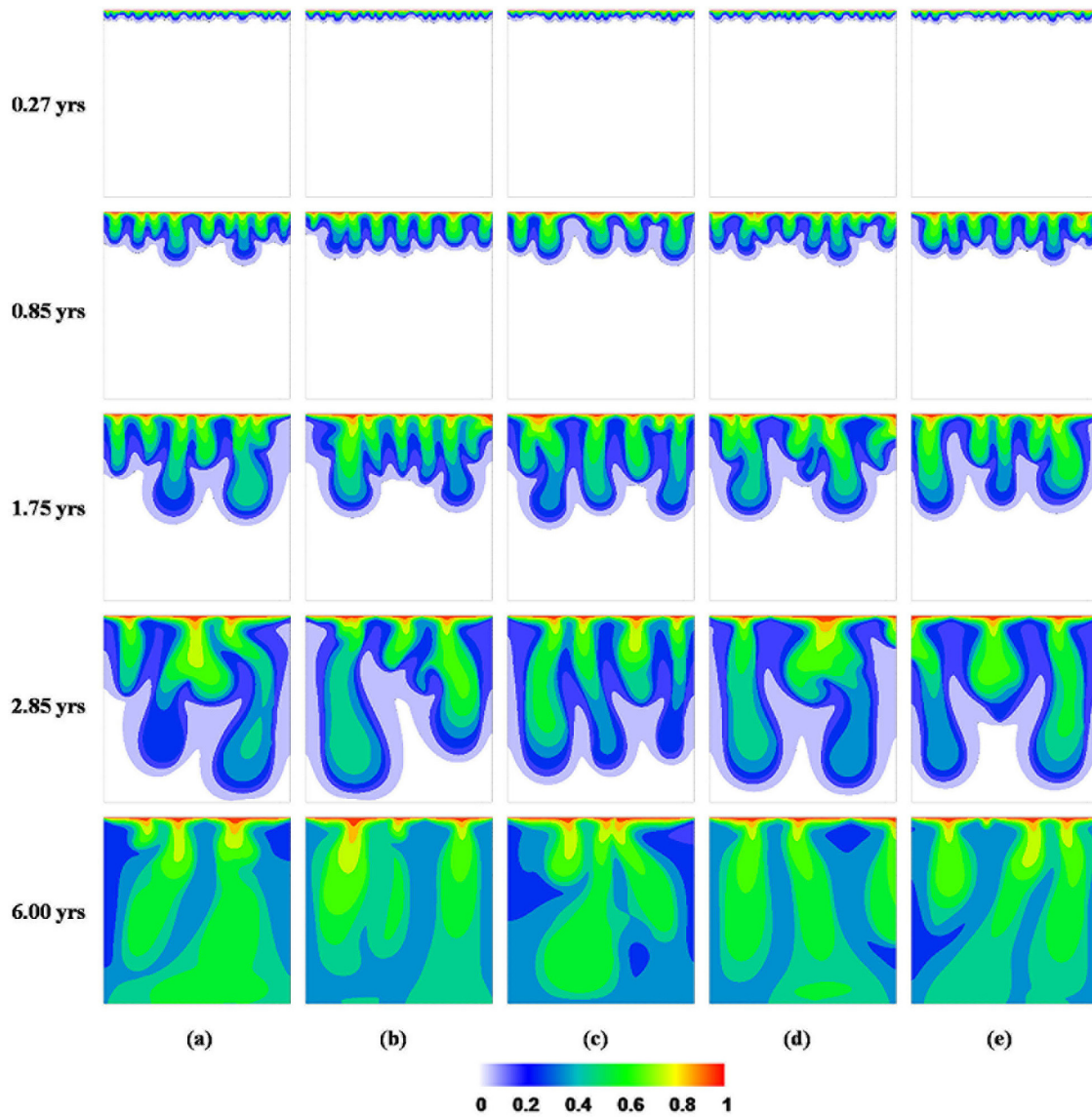
Figure 4. The demonstration of plume patterns in five different realizations of case BASE at various simulation times. Each column represents one realization of case BASE.
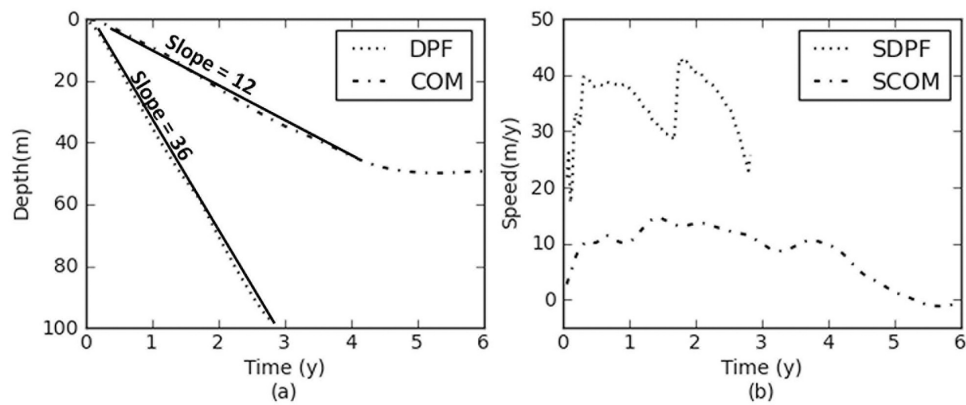

Figure 5. The development of quantitative diagnostics: (a) DPF and center of solute mass (COM) versus time and (b) instantaneous speed of DPF (SDPF) and instantaneous speed of COM (SCOM) versus time, corresponding to Figure 4a.
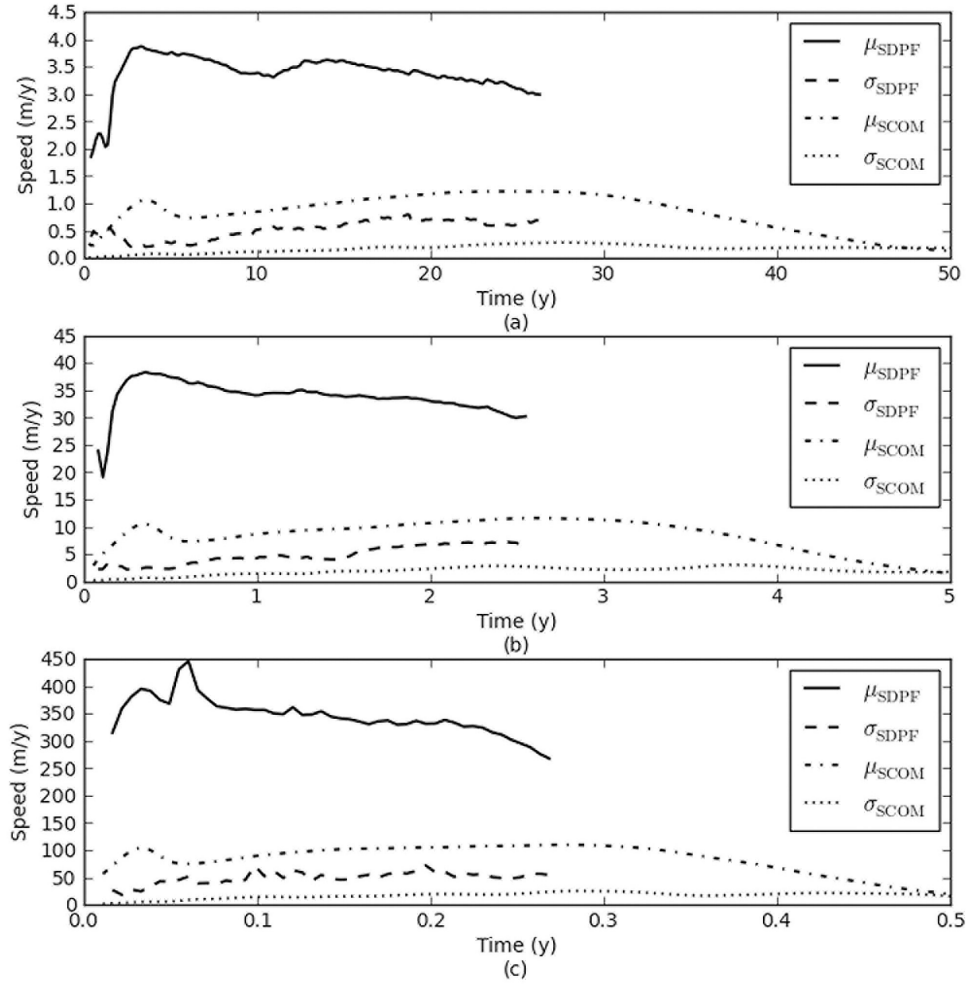
Figure 6. The variation in means and standard deviations of both SDPF and SCOM versus time in (a) case MP1 ($k = 4.85 \times 10^{-14}\,\mathrm{m}^2$), (b) case BASE ($k = 4.85 \times 10^{-13}\,\mathrm{m}^2$), and (c) case MP2 ($k = 4.85 \times 10^{-12}\,\mathrm{m}^2$).

because of the inherent highly nonlinear dynamics, but they do show very small standard deviation values compared to the corresponding mean at any specific time. For instance, the maximum σ_{SDPF} can be observed at 0.79 m yr^{-1} (μ_{SDPF} = 3.37 m yr^{-1}) at 18.63 years in case MP1, 7.22 m yr^{-1} (μ_{SDPF} = 30.49 m yr^{-1}) at 2.44 years in case BASE, and 72.12 m yr^{-1} (μ_{SDPF} = 331.21 m yr^{-1}) at 0.20 year in case MP2. The small variability in comparison to the mean values implies that (1) fingering speeds can be reasonably reproduced and (2) one single model can be utilized to predict, at least to a first-order estimate, the fingering speeds. It is also evident that σ_{SCOM} appears to be more stable and reliable than σ_{SDPF} because σ_{SCOM} tends to remain very close to 0 m yr^{-1}, meaning little variability in SCOM. Thus, a plume characteristic involving spatial integration may provide better prediction results than one that is sensitive to local-scale behavior (e.g., COM is better than DPF in a predictive sense).

3.3. The Effect of Effective Porosity ϵ

[38] Figure 8 presents the descent of DPF with time in three cases where ε was varied from BASE ($\varepsilon = 0.1$) to EP1 ($\varepsilon = 0.01$) and EP2 ($\varepsilon = 0.4$), respectively. Evidently, the increase in ε from case EP1 to cases BASE and EP2

caused the decrease in time for DPF to reach the bottom by nearly the same magnitude. For instance, DPF reached a depth of 80 m at 9.45, 2.35, and 0.25 years for $\varepsilon = 0.4$, 0.1, and 0.01, respectively. Even though fluctuations of fingering speeds can also be seen in Figure 8 from the DPF-time curve, the overall tendency can be linearly approximated as a constant SDPF and adequately utilized to elucidate the role of ε in controlling fingering speeds. Slopes (i.e., approximately 330.7, 33.6, and 8.3 m yr^{-1} corresponding to cases EP1, BASE, and EP2, respectively) therefore demonstrate that ε does have an inverse impact on fingering speeds and must therefore be incorporated into the denominator of fingering speed formula, as suspected. This is, however, not routinely done in the existing literature.

[39] The statistical results of fingering speeds in cases EP1 and EP2 demonstrate very similar trends to cases MP1 and MP2 and are therefore not shown here.

3.4. The Effect of Dispersion D_β

[40] Figure 9 illustrates the plume patterns of each realization of case MD1 ($\beta_{\mathrm{L}} = 1$ m, $\beta_{\mathrm{T}} = 0.1$ m) and case MD2 ($\beta_{\mathrm{L}} = 10$ m, $\beta_{\mathrm{T}} = 1$ m) at different times in comparison to case BASE ($\beta_{\mathrm{L}} = 1$ m, $\beta_{\mathrm{T}} = 1$ m). The reduction in
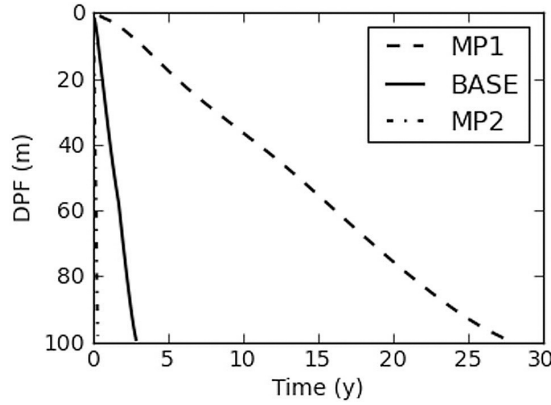
Figure 7. The comparison of DPF development based on one realization of cases MP1 ($k = 4.85 \times 10^{-14}$ m^2), BASE ($k = 4.85 \times 10^{-13}$ m^2), and MP2 ($k = 4.85 \times 10^{-12}$ m^2).

β_T weakened the lateral dissipation of the solute, thereby causing the formation of narrower fingers, as observed in Figure 9b, whereas the growth of β_L strengthened the vertical spread of solute such that fingers appeared to be more balloon shaped and dispersive (Figure 9c). The global fingering speeds of both cases seem to be slower than case BASE because DPF only penetrated around three quarters of the depth within 2.85 years (Figures 9b and 9c) by which time DPF in case BASE has reached the bottom of Figure 9a. The decrease in fingering speeds in case MD2 is intuitively reasonable because of the stronger dissipation capability of the system induced by the increase in β_L. However, the reduction in fingering speeds in case MD1 is somewhat counterintuitive as the smaller dissipation capability associated with the reduction in β_T should result in faster finger penetration. This phenomenon is probably attributed to a smaller density difference, indicated by lower solute contours within finger tips, because smaller β_T established narrower transport conduits, which allow only a small amount of solute mass to spread downward. The detailed analysis of the effects of dispersion is presented later in section 3.4.

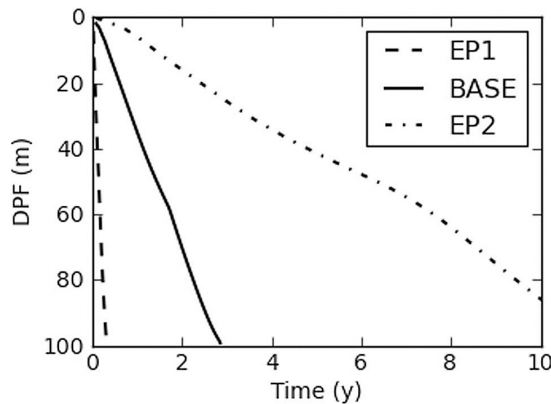[41] Figure 10 compares and contrasts mean speeds and the corresponding standard deviations of both SDPF and

Figure 8. The comparison of DPF development in cases with different effective porosity values: BASE ($\varepsilon = 0.1$), EP1 ($\varepsilon = 0.01$), and EP2 ($\varepsilon = 0.4$).
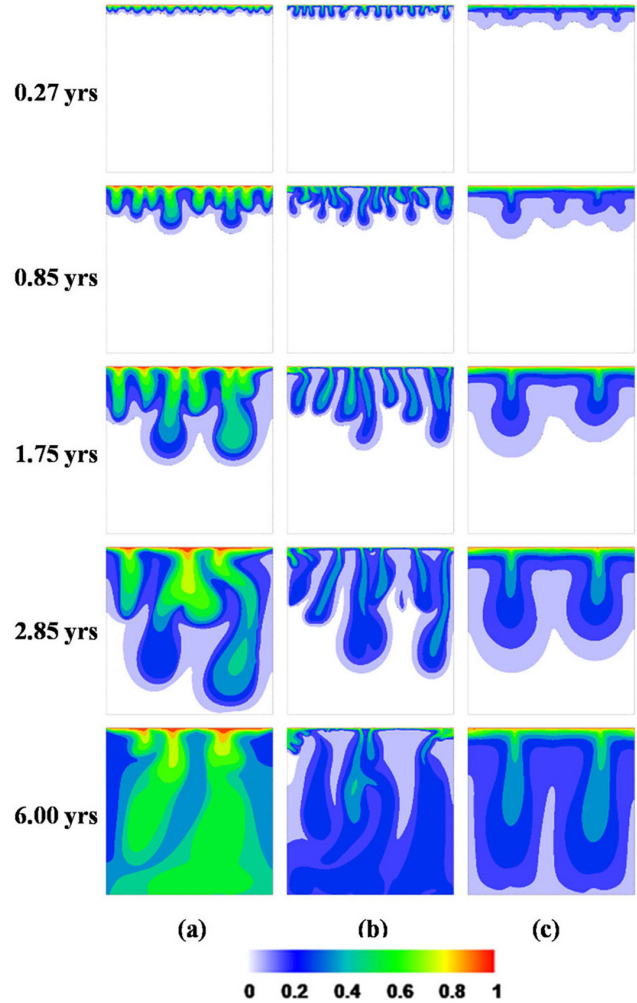

Figure 9. The demonstration of plume evolution in one realization of (a) case BASE ($\beta_L = 1$ m, $\beta_T = 1$ m), (b) case MD1 ($\beta_L = 1$ m, $\beta_T = 0.1$ m), and (c) case MD2 ($\beta_L = 10$ m, $\beta_T = 1$ m).

SCOM in cases BASE, MD1, and MD2. As expected, both cases MD1 and MD2 produced similar trends for μ_{SDPF} and μ_{SCOM} as case BASE during the period from the formation of relatively independent fingers to the time fingers reached the bottom (roughly from 0.5 to 3.5 years in Figures 9a and 9b). Consistent with the visual inspection in Figure 8, both the decrease in β_T to 0.1 m (case MD1) and the increase in β_L to 10 m (case MD2) from 1 m (case BASE) led to the decrease in μ_{SDPF} and μ_{SCOM}. However, unlike the response to variation in matrix permeability k and effective porosity ε, fingering speeds do not change dramatically in similar magnitudes to the change of dispersivities. This clearly demonstrates that fingering speeds are far less dependent on dispersivities than other parameters comprising $\mathbf{V_c}$. Dispersivity clearly appears to be a second-order effect.

[42] Both μ_{SDPF} and μ_{SCOM} demonstrate decreasing fingering speeds from relatively high speeds in cases MD1 and MD2 at the very beginning (from 0 to 0.5 year), as opposed to case BASE. This is mainly caused by the anisotropic dispersion (stronger vertically than laterally) by which fingers can be easily and quickly triggered by
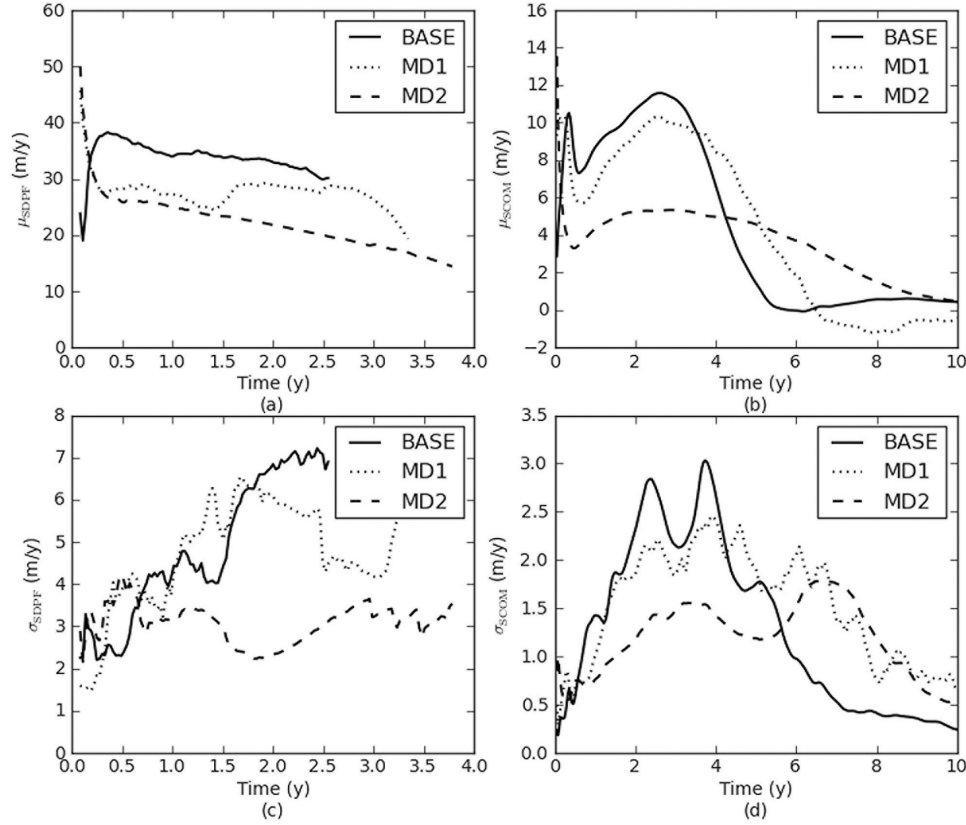
Figure 10. The comparison of means and standard deviations of SDPF and SCOM in cases BASE ($\beta_L = 1$ m, $\beta_T = 1$ m), MD1 ($\beta_L = 1$ m, $\beta_T = 0.1$ m), and MD2 ($\beta_L = 10$ m, $\beta_T = 1$ m): (a) μ_{SDPF} versus time, (b) μ_{SCOM} versus time, (c) σ_{SDPF} versus time, and (d) σ_{SCOM} versus time.

small perturbations once the boundary layer is established. Subsequently, lateral interaction retarded the penetration of fingers, thereby causing a reduction in fingering speeds.

[43] The later μ_{SCOM} starts to approach 0 m yr^{-1} asymptotically because of the accumulation of salt and stabilizing of plumes, but the time for μ_{SCOM} to reach 0 m yr^{-1} is dependent on the overall degree of fingering speeds; the comparison in Figure 10b shows that MD1 is preceded by BASE but followed by MD2, consistent with fingering speeds during the finger penetration period. Interestingly, SCOM in MD1 tends to asymptote to 0 m yr^{-1} from the negative direction. This is attributed to the relatively small dispersivities, which established small conduits to transport and accumulated salt at the bottom (comparing plume patterns at 6.0 years between Figures 9b and 9c).

[44] Figures 10c and 10d present the temporal variability of SDPF and SCOM, respectively. Neither plot reveals clear trends about the relationship between fingering speeds and dispersivity due to oscillatory behavior of σ_{SDPF} and σ_{SCOM}. However, as in the counterpart in Figure 6, both σ_{SDPF} and σ_{SCOM} here also show very arbitrary but small variability at all times (maximum of 7.22 m yr^{-1} in Figure 10c and maximum of 3.03 m yr^{-1} in Figure 10d), independent of the choice of dispersivity values. This implies that irrespective of β_L and β_T values, there is good reproducibility and predictive capability for fingering speeds in the form of SDPF and SCOM, and SCOM appears to be more reliable than SDPF because of the integrating effect, consistent with earlier results in section 3.2.

[45] Table 2 presents statistical results of both U_{DPF} and U_{COM} through linear approximation in order to further

Table 2. Statistical Results of Fingering Speeds of Both U_{DPF} and U_{COM} With Various Longitudinal Dispersivity β_L and Transverse Dispersivity β_T Through Linear Approximation[a]

| | β_L (m) | | | | | |
| | 1 | | 5 | | 10 | |
β_T (m)	U_{DPF} (m yr^{-1})	U_{COM} (m yr^{-1})	U_{DPF} (m yr^{-1})	U_{COM} (m yr^{-1})	U_{DPF} (m yr^{-1})	U_{COM} (m yr^{-1})
0.1	MD1, 27.25 (2.13)	MD1, 8.82 (0.76)				
0.5	MD4, 33.42 (2.97)	MD4, 11.74 (0.94)	MD3, 21.92 (2.23)	MD3, 7.56 (1.11)		
1	BASE, 33.24 (3.06)	BASE, 10.10 (1.03)	MD5, 24.82 (2.05)	MD5, 8.38 (0.93)	MD2, 20.70 (2.44)	MD2, 4.99 (0.85)

[a]In each case, the mean value is presented after the model name and followed by the standard deviation value in parentheses.

elucidate the general trends of the relationship between D_β and fingering speeds. Several features can be observed from the results: (1) both $\sigma(U_{\mathrm{DPF}})$ and $\sigma(U_{\mathrm{COM}})$ are relatively small compared to $\mu(U_{\mathrm{DPF}})$ and $\mu(U_{\mathrm{COM}})$, respectively, consistent with previous results of SDPF and SCOM; (2) $\mu(U_{\mathrm{COM}})$ appears to be 3 times lower than $\mu(U_{\mathrm{DPF}})$, consistent with Figure 10; (3) increasing β_{L} (third row of Table 2) leads to the reduction of fingering speeds; (4) increasing β_{T} (first column) results in the increase followed by slight decrease in fingering speeds; (5) increasing both longitudinal and transverse dispersivities by the same magnitude together can cause the growth of fingering speeds (from MD2 to MD3 and MD1 diagonally upward). It is clear that β_{L} plays a more important role than β_{T} because it causes a direct impact on the dissipation of solute along the pathways of finger movement. More importantly, varying β_{L} and β_{T} together or individually by an order of magnitude does not cause significant differences in fingering speeds (there is approximately a factor of 2 between maximum and minimum mean speeds for both U_{DPF} and U_{COM}). In comparison to the effect of the hydraulic conductivity (varying with orders of magnitude difference), the dispersion effect is much weaker and does not contribute to the bulk portion of the variability of fingering speeds, and therefore, a factor of 2 in dispersion-induced variability is probably acceptable. This implies that fingering speeds can be accurately predicted provided that the hydraulic conductivity and porosity are well known. The uncertainty or variability seen in all the diagnostics here is probably relatively small when compared to the inherent uncertainty in hydraulic conductivity measurements in practice.

3.5. The Importance of the Density Effect

[46] *Simmons* [2005] stressed the importance of variable density flow by stating that only 5% of seawater (35,000 mg L^{-1}) salinity is required to achieve the equivalent driving force as a typical advective hydraulic gradient $I_0 = 0.001$ (1 m head difference over a distance of 1000 m). In the current study, the saltwater density (1200 kg m^{-3}) is equivalent to a salinity of 360,000 mg L^{-1} (an order of magnitude higher than seawater) and is typically found at sabkhas and playa lakes [e.g., *Van Dam et al.*, 2009]. This generates the equivalent driving density gradient $I_1 = \Delta\rho/\rho_0 = 0.200$, which is much stronger than I_0. Hence, this high density gradient is expected to play a much more significant role in causing groundwater flow and solute transport than typical advective hydraulic gradients.

[47] The relative importance of density effects was investigated through obtaining the equivalent advective hydraulic gradient required to generate the same average linear velocity through advection as a fingering speed driven by the density difference. The linear approximation result of SDPF (36 m yr^{-1}) in one realization of case BASE in Figure 5a is taken as an example. By substituting this SDPF and the corresponding matrix permeability (4.85 $\times$ 10^{-13} m^2) and porosity (0.1) into the average linear velocity, the equivalent advective hydraulic gradient can be obtained as $I_2 = 0.024$, an order of magnitude smaller than I_1. The large discrepancy between I_1 and I_2 indicates that in order to achieve a fingering speed of the same magnitude as an advective speed, the density gradient should be approximately 10 times greater than the corresponding hydraulic gradient. The ratio of I_2 to I_1 (0.12) is a corrective factor f applied to adjust the theoretical fingering speed V_c to a real fingering speed in this specific realization of case BASE, i.e., real speed of fingering is $f \times V_c$; f is upper bounded by 1 in accordance with the characteristic convective velocity (equation (A4)). The need for f arises because of several physical phenomena, including (1) fluid entrainment of individual fingers holding back the movement of fingers, (2) mechanical dispersion and molecular diffusion reducing the density difference within fingers, and (3) upwelling of fluid between neighboring fingers, which retards the penetration of fingers. Furthermore, it should be indicated that f is also impacted by the pressure (or potential) gradient, which is commonly small in free convection but cannot be zero. Without the pressure gradient occurring in all coordinate directions, fingering (recirculation pattern of flow) and any descent could not establish. This is a physical constraint caused by mass and momentum conservation and is always opposite to the density gradient in the vertical direction.

[48] The corrective factor f was further explored in Figure 11, which demonstrates the relationship between linearly approximated U_{DPF} and U_{COM} and the corresponding V_c from all simulations. Clearly, all results lie in the bottom right triangle zone of each graph and therefore indicate that fingering speeds are always smaller than the theoretical value of V_c. The slopes of the trends provide general corrective factors of 0.115 for U_{DPF} and 0.034 for U_{COM}, where U_{DPF} is comparatively 3 times greater than U_{COM}, consistent with previous results.

[49] It should be mentioned that this corrective factor of U_{DPF} ($f = 0.115$) is around half of the value ($f = 0.22$) derived by *Post and Kooi* [2003] and about one fourth of the value ($f = 0.446$) derived by *Wooding* [1969]. The discrepancies in f most likely stem from the differences in hydrogeologic settings, choice of measurable quantities, and scale geometries. It is, however, clear that all existing f values are lower than 1 (representing the theoretical fingering speed), and they surprisingly appear to be within the same comparable order of magnitude across different scales and systems. Given the complexity of free convection, it is impossible to find a universal f that is applicable to all settings. Therefore, the current corrected fingering speed (0.115 V_c) and the theoretical fingering speed (V_c) may provide guidance on the lower bound and upper bound of generic speeds of finger fronts. Both bounds are extremely helpful for establishing first-order intuition for fingering speeds and for designing measurements in laboratory and field experiments; that is, the upper bound can be used to design the frequency of the measurement, while the lower bound can be used to determine the length of the measurement of experimentation. Note that the effective V_c is not appropriate for assessing seawater intrusion speed because the velocity direction of the salinity wedge (horizontal) is not aligned with the gravity direction (vertical).

[50] A preliminary comparison between 2-D and 3-D models was conducted. Quantitative results of 3-D models appear to be close to those of 2-D models on the basis of a single simulation. However, this is computationally prohibitive, and it is hard to produce statistical results at this time because of the stochastic nature of the study and the computational burden associated with each numerical simulation. Further study of 3-D effects in a stochastic framework
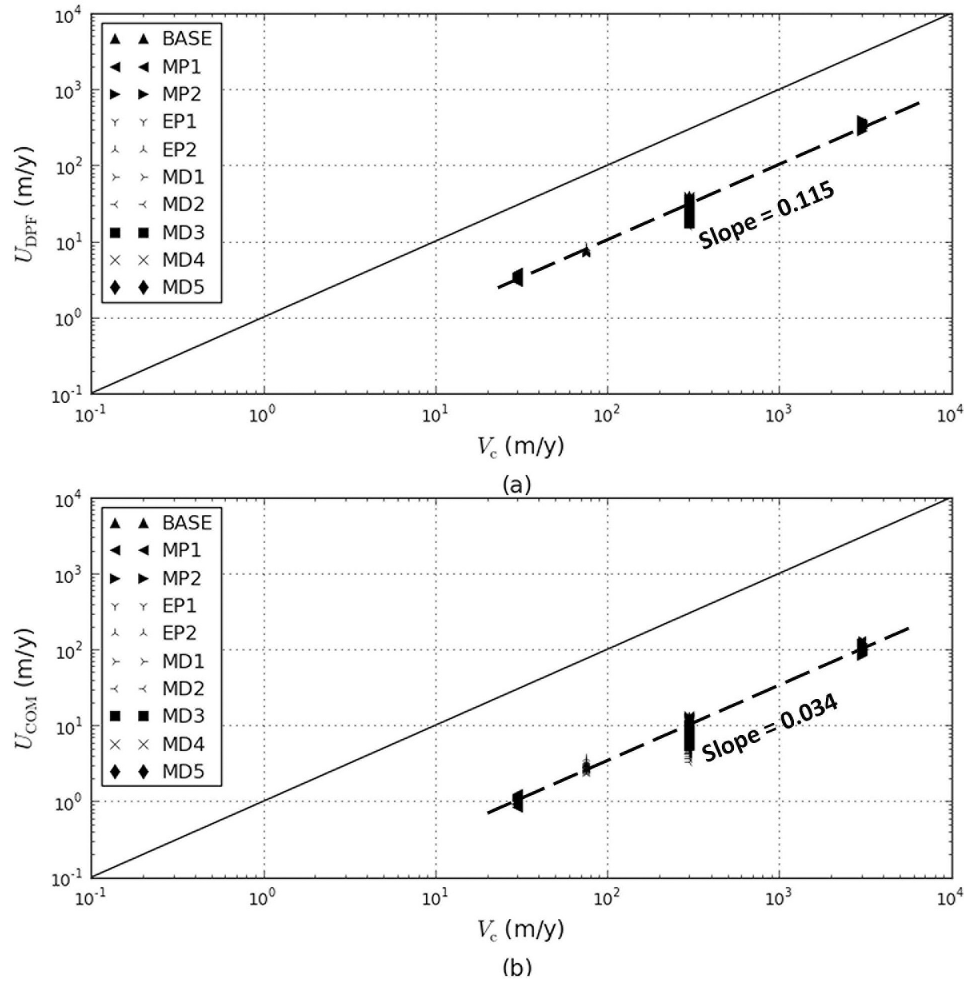
Figure 11. The demonstration of relationships between (a) U_{DPF} and $\mathbf{V_c}$ and (b) U_{COM} and $\mathbf{V_c}$. Both U_{DPF} and U_{COM} are derived through the linear approximation approach.

is warranted to investigate fingering speeds in larger length and time scales.

4. Summary and Conclusions

[51] Understanding the speed of free convective fingering is important because it can establish fundamentally significant intuition to predict the movement of unstable fingers and provide guidance on detecting and/or monitoring field-based transient free convective behavior. There has been ongoing ambiguity regarding how to calculate the speed of free convective fingering and in understanding what the likely rates of fingering are in real field settings. Unlike advective processes, the intuition and understanding surrounding the speed of free convection processes in groundwater are lacking. This is important for understanding and predicting free convection processes in modeling, laboratory, and field-scale settings. This paper has studied the effect of different parameters on the speed of free convective fingering in porous media using numerical simulations. The fingering speeds were measured and analyzed in the form of two important characteristics, deepest plume front (DPF) and vertical center of solute mass (COM). A

perturbation-based stochastic approach was applied to explore the variability of fingering speeds by quantifying mean and standard deviation values of both descent rates of DPF and COM (SDPF and SCOM, respectively) at different times. We conclude our study with the following remarks.

[52] 1. Fingering speeds are dependent on various measurable diagnostics that are characterized by continuous vertical penetration due to the density effect (e.g., DPF and COM), and therefore, a free convective system may produce a spectrum of fingering speeds that is a function of measured diagnostics. It is observed that DPF monitoring of the behavior of the most advanced interface between saltwater and fresh water yields an upper bound of the spectrum of fingering speeds, whereas COM displays a global trend of fingering speeds that is always smaller than that obtained from analysis of DPF.

[53] 2. On the basis of a linear approximation, both DPF and COM yield relatively constant fingering speeds during the vigorous finger penetration period (i.e., from the time relatively discrete and independent fingers are formed to the time finger tips reach the bottom of the system). But analysis of instant speeds shows that the speed of DPF (SDPF) tends to decelerate because of the sensitivity to the

bottom boundary effect that constrains the fluid flow field, while the speed of COM (SCOM) tends to accelerate because of continuous reinforcement from the source zone.

[54] 3. Hydrogeologic parameters (permeability and porosity) play significant roles in fingering speeds and must necessarily be included to formulate the theoretical fingering speed in a similar fashion to a hydraulically driven average linear velocity. Dispersion is also seen to be a second-order effect (much weaker than permeability and porosity) on fingering speeds. How the dispersion coefficient can be included in the formula of the theoretical fingering speed requires further systematic investigation.

[55] 4. Because of dispersion-diffusion, fluid entrainment, and upwelling effects, the real fingering speeds are always slower than the V_c. Therefore, V_c cannot be utilized to predict a real fingering speed in a system unless being evaluated in association with a corrective factor f, which is likely to be around $f = 0.115$ for DPF and $f = 0.034$ for COM on the basis of linear approximation in the current study. Given the complexity of free convection, we acknowledge that it is impossible to find a universal f, and therefore, the current f is not generalizable to all various settings. However, in combination with previous studies [*Wooding*, 1969; *Post and Kooi*, 2003], f for speeds of the finger front is most likely to be constrained by (0.115, 1.000), which is extremely helpful for establishing the first-order intuition and designing the measurement of laboratory and field experiments. The upper bound (1.000) can be used to design the frequency of the measurements on the basis of the higher-speed estimate, while the lower bound (0.115) based on the lower-speed estimate can be used to determine the length of the overall experimental time run. These are useful bounds for experimental design.

[56] 5. A perturbation-based stochastic analysis has demonstrated that a single numerical model can be adopted to predict the approximate speed of free convective fingering because of the surprisingly small variability in both SDPF and SCOM at all times. This critically indicates that fingering speeds can be reasonably reproduced and are more predictable than may be suggested by their very complex and semichaotic behavior. However, as it is commonly recognized, the strongest uncertainty in hydrogeology stems from the uncertainty in hydraulic conductivity, which may vary over several orders of magnitude. In comparison to the variability of both SDPF and SCOM seen in this study, the uncertainty of hydraulic conductivity is by far expected to be the most significant contributor to the uncertainty in fingering speeds. Therefore, if the hydraulic conductivity can be accurately determined in the field, we expect that we can make good predictions of fingering speeds with a single realization of the system. This is an important finding because it has not been evident in the literature whether or not fingering speeds are reproducible and amenable to prediction.

[57] This study provides new insights into finger descent by analyzing and clarifying the roles of different parameters. The results can assist us in establishing a priori intuition about the speed of free convective fingering and predicting free convection behavior, which will ultimately be useful for designing systems to monitor the transient fingering behavior associated with environmental phenomena. Further work should be undertaken to investigate the effects of source length scales (e.g., representing different sabkha scales and acting as a top concentration boundary condition), mass supply time scales (e.g., representing periods of saline inundations) on fingering speeds, and the dimensionality effect in 3-D models.

Appendix A: The Derivation of the Characteristic Convective Velocity

[58] Darcy's law considering density effect is formulated as

$$\mathbf{q} = -K \cdot \left(\nabla h + \frac{\Delta \rho}{\rho_0} \mathbf{e} \right), \tag{A1}$$

where $\mathbf{q} = \varepsilon \mathbf{v}$ is the Darcy velocity (a specific bulk flux), with ε being effective porosity and $\mathbf{v}$ being the pore (intrinsic) velocity; K is the hydraulic conductivity, ∇h is the potential head gradient, $\Delta \rho$ is the density difference between maximum density and base reference density, and $\mathbf{e} = -g/||g||$ is the gravitational unit vector. Assuming fluid flow occurs in the gravity direction (i.e., g is aligned with the vertical z axis) of a homogeneous and isotropic porous medium and assuming there is no potential head gradient, we obtain

$$\mathbf{q} = \begin{bmatrix} q_x \\ q_y \\ q_z \end{bmatrix} = -K \begin{bmatrix} 0 \\ 0 \\ \Delta \rho / \rho_0 \end{bmatrix}. \tag{A2}$$

[59] This can be written in a simplified form to derive the characteristic convective (Darcy) velocity:

$$\mathbf{U_c} = |q_z| = K \frac{\Delta \rho}{\rho_0}. \tag{A3}$$

[60] Usually, the intrinsic pore velocity is the right quantity to measure instead of the bulk Darcy velocity. Therefore, the characteristic convective velocity is given by dividing ε:

$$\mathbf{V_c} = |q_z / \varepsilon| = \frac{K}{\varepsilon} \frac{\Delta \rho}{\rho_0}. \tag{A4}$$

Appendix B: FEFLOW Governing Flow and Transport Equations

[61] The governing equations in FEFLOW [*Diersch*, 2005] are composed of fluid mass, momentum, and solute mass conservation equations. The fluid mass conservation equation is given by

$$\frac{\partial (\varepsilon \rho)}{\partial t} + \nabla \cdot (\varepsilon \rho \mathbf{v}) = \varepsilon \rho Q_\rho, \tag{B1}$$

where ε is the effective porosity, ρ is the fluid density, and Q_ρ is the fluid mass source or sink. It is assumed that density is linearly proportional to concentration:

$$\rho = \rho_0 \left(1 + \frac{\bar{\alpha}}{C_s - C_0} (C - C_0) \right), \tag{B2}$$

where ρ_0 is the initial density corresponding to the initial concentration C_0, C is the concentration, C_s is the maximum

concentration, and $\bar{\alpha}$ is the density difference ratio between maximum density and base reference density.

[62] The momentum conservation equation (i.e., Darcy's law) is given by

$$\mathbf{v} + \frac{k}{\varepsilon\mu} \cdot (\nabla p - \rho g) = 0, \tag{B3}$$

where k is intrinsic permeability, μ is the dynamic viscosity, p is fluid pressure, and g is acceleration due to gravity.

[63] The solute mass conservation equation is given by

$$\frac{\partial(\varepsilon C)}{\partial t} + \nabla \cdot (\varepsilon C\mathbf{v}) + \nabla \cdot \mathbf{j} = Q_c, \tag{B4}$$

where Q_c is the solute mass source or sink and $\mathbf{j}$ is the Fickian mass flux governed by Scheidegger-Bear's dispersion approach:

$$\mathbf{j} = -\varepsilon \left[(D_0 + \beta_{\mathrm{T}} \|\mathbf{v}\|)\mathbf{I} + (\beta_{\mathrm{L}} - \beta_{\mathrm{T}}) \frac{\mathbf{v} \otimes \mathbf{v}}{\|\mathbf{v}\|} \right] \cdot \nabla C, \tag{B5}$$

where D_0 is the molecular diffusion coefficient, β_{L} and β_{T} are the longitudinal dispersivity and transverse dispersivity, respectively, and $\mathbf{I}$ is the unit (identity) tensor.

Appendix C: Mathematical Definitions of Diagnostics

[64] The mathematical definition of COM is given as

$$\mathrm{COM} = \frac{1}{M} \int \rho(y) y \, \mathrm{d}V, \tag{C1}$$

where M is the total solute mass and $\rho(y)$ is the integral density at the depth y. Instant speeds of DPF and COM are given by

$$\mathrm{SDPF} = \frac{\mathrm{d\,DPF}}{\mathrm{d}t} \tag{C2}$$

$$\mathrm{SCOM} = \frac{\mathrm{d\,COM}}{\mathrm{d}t}. \tag{C3}$$

[65] The mean and standard deviation of SDPF are given by

$$\mu_{\mathrm{SDPF}} = \frac{\sum\limits_{i=1}^{n} (\mathrm{SDPF})_i}{n} \tag{C4}$$

$$\sigma_{\mathrm{SDPF}} = \sqrt{\frac{\sum\limits_{i=1}^{n} \left[(\mathrm{SDPF})_i - \mu_{\mathrm{SDPF}} \right]^2}{n-1}}, \tag{C5}$$

where n is the number of samples in a set of models; $n = 30$ in this study. The mean and standard deviation of SCOM are given by

$$\mu_{\mathrm{SCOM}} = \frac{\sum\limits_{i=1}^{n} (\mathrm{SCOM})_i}{n} \tag{C6}$$

$$\sigma_{\mathrm{SCOM}} = \sqrt{\frac{\sum\limits_{i=1}^{n} \left[(\mathrm{SCOM})_i - \mu_{\mathrm{SCOM}} \right]^2}{n-1}}. \tag{C7}$$

Notation

x, y horizontal and vertical spatial coordinates, respectively [L].

$\Delta x, \Delta y$ horizontal and vertical element sizes, respectively [L].

ΔL transport distance between two sides of an element measured in the direction of groundwater flow [L].

H, L depth and length of a model, respectively [L].

k permeability of a porous medium [L^2].

∇h potential head gradient (dimensionless).

g gravitational acceleration [$L\,T^{-2}$].

$\mathbf{e}$ gravitational unit vector, equal to $-g/\|g\|$ (dimensionless).

μ dynamic viscosity [$M\,L^{-1}\,T^{-1}$].

ε effective porosity (dimensionless).

ρ_0 base reference fluid density [$M\,L^{-3}$].

ρ fluid density [$M\,L^{-3}$].

$\Delta\rho$ density difference between maximum density and base reference density [$M\,L^{-3}$].

$\bar{\alpha}$ density difference ratio of density difference to base reference density (dimensionless).

K hydraulic conductivity of a porous medium [$L\,T^{-1}$].

C_0 normalized base reference concentration (dimensionless).

C normalized fluid concentration (dimensionless).

C_s normalized maximum concentration (dimensionless).

$C_{\mathrm{node}}(t)$ normalized concentration of a node at the top boundary at time t (dimensionless).

C_{dense} normalized concentration of dense water (dimensionless).

rand $(t,0)$ random function used for generating fractions uniformly distributed between 0 and 1 (dimensionless).

Q_ρ fluid mass source or sink [T^{-1}].

Q_c solute mass source or sink [$M\,L^{-3}\,T^{-1}$].

j Fickian mass flux [$M\,L^{-2}\,T^{-1}$].

$\mathbf{q}$ Darcy velocity [$L\,T^{-1}$].

$\mathbf{v}$ pore (intrinsic) velocity [$L\,T^{-1}$].

$\mathbf{U_c}$ generalized characteristic convective (Darcy) velocity [$L\,T^{-1}$].

$\mathbf{V_c}$ characteristic convective velocity [$L\,T^{-1}$].

p fluid pressure [$M\,L^{-1}\,T^{-2}$].

Ra nondimensional Rayleigh number (dimensionless).

D_0 molecular diffusion coefficient [$L^2\,T^{-1}$].

β_{L} longitudinal dispersivity [L].

β_{T} transverse dispersivity [T].

T time scale of a model [T].

Pe mesh Péclet number (dimensionless).

$\mathbf{I}$ unit (identity) tensor (dimensionless).

M total solute mass [$M\,L^{-3}$].

f corrective factor (dimensionless).

n	number of samples in a set of models (dimensionless).
DPF	deepest plume front $[L]$.
COM	vertical center of solute mass $[L]$.
SDPF	the instantaneous speed of DPF $[L\ T^{-1}]$.
SCOM	the instantaneous speed of COM $[L\ T^{-1}]$.
μ_{SDPF}	mean of SDPF $[L\ T^{-1}]$.
σ_{SDPF}	standard deviation of SDPF $[L\ T^{-1}]$.
μ_{SCOM}	mean of SCOM $[L\ T^{-1}]$.
σ_{SCOM}	standard deviation of SCOM $[L\ T^{-1}]$.
U_{DPF}	linear approximation of the speed of DPF $[L\ T^{-1}]$.
U_{COM}	linear approximation of the speed of COM $[L\ T^{-1}]$.
$\mu(U_{\text{DPF}})$	mean of U_{DPF} $[L\ T^{-1}]$.
$\mu(U_{\text{COM}})$	mean of U_{COM} $[L\ T^{-1}]$.
$\sigma(U_{\text{DPF}})$	standard deviation of U_{DPF} $[L\ T^{-1}]$.
$\sigma(U_{\text{COM}})$	standard deviation of U_{COM} $[L\ T^{-1}]$.

References

Ackerer, P., A. Younes, and R. Mose (1999), Modeling variable density flow and solute transport in porous medium: 1. Numerical model and verification, *Transp. Porous Media*, 35, 345–373.

Adams, J. J., and S. Bachu (2002), Equations of state for basin geofluids: Algorithm review and intercomparison for brines, *Geofluids*, 2, 257–271.

Bear, J. (1972), *Dynamics of Fluids in Porous Media*, Elsevier, New York.

Diersch, H. J. G. (2005), FEFLOW: Finite element subsurface flow & transport simulation system, software, WASY GmbH, Inst. for Water Resour. Plann. and Syst. Res., Berlin.

Diersch, H. J. G., and O. Kolditz (2002), Variable-density flow and transport in porous media: Approaches and challenges, *Adv. Water Resour.*, 25, 899–944.

Elder, J. W. (1967), Transient convection in a porous medium, *J. Fluid. Mech.*, 27(3), 609–623.

Gebhart, B., Y. Jaluria, R. L. Mahajan, and B. Sammakia (1988), *Buoyancy Induced Flows and Transport*, Hemisphere, Washington, D. C.

Horne, R. N., and J. Caltagirone (1980), On the evolution of thermal disturbances during natural convection in a porous medium, *J. Fluid. Mech.*, 100(2), 385–395.

Juster, T., P. A. Kramer, H. L. Vacher, P. K. Swart, and M. Stewart (1997), Groundwater flow beneath a hypersaline pond, Cluett Key, Florida Bay, Florida, *J. Hydrol.*, 197, 339–369.

Kolditz, O., R. Ratke, H. J. G. Diersch, and W. Zielke (1998), Coupled groundwater flow and transport: 1. Verification of variable-density flow and transport models, *Adv. Water Resour.*, 21, 27–46.

Kreyszig, E. (1988), *Advanced Engineering Mathematics*, 6th ed., John Wiley, New York.

Moortgat, J., S. Sun, and A. Firoozabadi (2011), Compositional modeling of three-phase flow with gravity using higher-order finite element methods, *Water Resour. Res.*, 47, W05511, doi:10.1029/2010WR009801.

Oldenburg, C. M., and K. Pruess (1995), Dispersive transport dynamics in a strongly coupled groundwater–brine flow system, *Water Resour. Res.*, 31(2), 289–302, doi:10.1029/94WR02272.

Oostrom, M., J. S. Hayworth, J. H. Dane, and O. Guven (1992), Behavior of dense aqueous phase leachate plumes in homogeneous porous media, *Water Resour. Res.*, 28(8), 2123–2134, doi:10.1029/92WR00711.

Post, V., and C. Simmons (2010), Free convective controls on sequestration of salts into low-permeability strata: Insights from sand tank laboratory experiments and numerical modelling, *Hydrogeol. J.*, 18, 39–54, doi:10.1007/s10040-009-0521-4.

Post, V. E. A., and H. Kooi (2003), Rates of salinization by free convection in high-permeability sediments: Insights from numerical modeling and application to the Dutch coastal area, *Hydrogeol. J.*, 11, 549–559.

Post, V. E. A., and H. Prommer (2007), Multicomponent reactive transport simulation of the Elder problem: Effects of chemical reactions on salt plume development, *Water Resour. Res.*, 43, W10404, doi:10.1029/2006WR005630.

Prasad, A., and C. T. Simmons (2003), Unstable density-driven flow in heterogeneous porous media: A stochastic study of the *Elder* [1967b] "short heater" problem, *Water Resour. Res.*, 39(1), 1007, doi:10.1029/2002WR001290.

Riaz, A., M. Hesse, H. A. Tchelepi, and F. M. Orr Jr. (2006), Onset of convection in a gravitationally unstable diffusive boundary layer in porous media, *J. Fluid. Mech.*, 548, 87–111.

Schincariol, R. A., and F. W. Schwartz (1990), An experimental investigation of variable density flow and mixing in homogeneous and heterogeneous media, *Water Resour. Res.*, 26(10), 2317–2329, doi:10.1029/WR026i010p02317.

Schulze-Makuch, D. (2005), Longitudinal dispersivity data and implications for scaling behaviour, *Ground Water*, 43(3), 443–456.

Simmons, C. T. (2005), Variable density groundwater flow: From current challenges to future possibilities, *Hydrogeol. J.*, 13, 116–119.

Simmons, C. T., K. A. Narayan, and R. A. Wooding (1999), On a test case for density-dependent groundwater flow and solute transport models: The salt lake problem, *Water Resour. Res.*, 35(12), 3607–3620, doi:10.1029/1999WR900254.

Simmons, C. T., M. L. Pierini, and J. L. Hutson (2002), Laboratory Investigation of variable-density flow and solute transport in unsaturated-saturated porous media, *Transp. Porous Media*, 47, 215–244.

Stevens, J. D., J. M. Sharp Jr., C. T. Simmons, and T. R. Fenstemaker (2009), Evidence of free convection in groundwater: Field-based measurements beneath wind-tidal flats, *J. Hydrol.*, 375, 394–409.

Van Dam, R. L., C. T. Simmons, D. W. Hyndman, and W. W. Wood (2009), Natural free convection in porous media: First field documentation in groundwater, *Geophys. Res. Lett.*, 36, L11403, doi:10.1029/2008GL036906.

van Reeuwijk, M., S. A. Mathias, C. T. Simmons, and J. D. Ward (2009), Insights from a pseudospectral approach to the Elder problem, *Water Resour. Res.*, 45, W04416, doi:10.1029/2008WR007421.

Voss, C. I., and W. R. Souza (1987), Variable density flow and solute transport simulation of regional aquifers containing a narrow freshwater-saltwater transition zone, *Water Resour. Res.*, 23(10), 1851–1866, doi:10.1029/WR023i010p01851.

Wooding, R. A. (1969), Growth of fingers at an unstable diffusing interface in a porous medium or Hele-Shaw cell, *J. Fluid. Mech.*, 39(3), 477–495.

Wooding, R. A., S. W. Tyler, and I. White (1997), Convection in groundwater below an evaporating salt lake: 1. Onset of instability, *Water Resour. Res.*, 33(6), 1199–1217, doi:10.1029/96WR03533.

Xie, Y., C. T. Simmons, A. D. Werner, and J. D. Ward (2010), Effect of transient solute loading on free convection in porous media, *Water Resour. Res.*, 46, W11511, doi:10.1029/2010WR009314.

Zhang, H., and F. W. Schwartz (1995), Multispecies contaminant plumes in variable density flow systems, *Water Resour. Res.*, 31(4), 837–847, doi:10.1029/94WR02567.

Zimmermann, S., P. Bauer, R. Held, W. Kinzelbach, and J. H. Walther (2006), Salt transport on islands in the Okavango Delta: Numerical investigations, *Adv. Water Resour.*, 29, 11–29.

C. T. Simmons, A. D. Werner, and Y. Xie, National Centre for Groundwater Research and Training, Flinders University, GPO Box 2100, Adelaide, SA 5001, Australia. (yueqing.xie@flinders.edu.au)